Applied Catalysis B: Environmental 323 (2023) 122190

Contents lists available at ScienceDirect

Applied Catalysis B: Environmental

journal homepage: www.elsevier.com/locate/apcatb

The dual-active-site tandem catalyst containing Ru single atoms and Ni nanoparticles boosts CO_2 methanation

Tengfei Zhang [a,b,c,1], Peng Zheng [d,1], Fangna Gu [a,*], Wenqing Xu [a,*], Wenxing Chen [e,*], Tingyu Zhu [a], Yi-Fan Han [f], Guangwen Xu [d,g], Ziyi Zhong [b,h,**], Fabing Su [a,g,***]

[a] Institute of Process Engineering, Chinese Academy of Sciences, Beijing 100190, China
[b] Guangdong Provincial Key Laboratory of Materials and Technologies for Energy Conversion (MATEC), GTIIT, Guangdong 515063, China
[c] School of Chemical Engineering, University of Chinese Academy of Sciences, Beijing 100049, China
[d] Key Laboratory on Resources Chemicals and Materials of Ministry of Education, Shenyang University of Chemical Technology, Shenyang 110142, China
[e] Energy & Catalysis Center, School of Materials Science and Engineering, Beijing Institute of Technology, Beijing 100081, China
[f] State Key Laboratory of Chemical Engineering, School of Chemical Engineering, East China University of Science and Technology, Shanghai 200237, China
[g] Institute of Industrial Chemistry and Energy Technology, Shenyang University of Chemical Technology, Shenyang 110142, China
[h] Department of Chemical Engineering, Guangdong Technion Israel Institute of Technology (GTIIT), 241 Daxue Road, Shantou 515063, China

ARTICLE INFO

Keywords:
Dual active sites
Tandem catalyst
Ru single atoms
Ni nanoparticles
CO_2 methanation

ABSTRACT

Hydrogenation of CO_2 into CH_4 is an effective strategy for dealing with CO_2-relevant environmental problems. Since the CO_2 methanation reaction involves multiple electron transfers and various C1 intermediates, improving the reaction rate at each step is critical to accelerating the entire reaction. Here, we report a dual-active-site tandem catalyst (Ru_1Ni/CeO_2) composed of Ru single atoms (Ru_1) and Ni nanoparticles, which can effectively convert CO_2 to CH_4, showing ~90% CO_2 conversion and ~99% CH_4 selectivity at 325 °C, much higher than those of the Ru_1/CeO_2 and Ni/CeO_2 catalysts. Experimental and theoretical calculation results reveal that Ru_1 is extremely active for converting CO_2 to CO, while the Ni site is highly efficient for the subsequent sequential CO to CH_4 reaction step. The coexistence of the Ru_1 and Ni sites significantly boosts the overall reaction. This work offers a promising strategy for the rational design of efficient multisite tandem catalysts.

1. Introduction

Directly converting CO_2 from fossil fuel combustion into high-value-added products can address environmental problems and the energy crisis [1–5]. In particular, reducing CO_2 to CH_4 at atmospheric pressure is attractive [6]. Compared to the electro-reduction and photo-reduction of CO_2 to CH_4 [7–9], the thermal-reduction catalytic process (CO_2 methanation) with the higher one-way CO_2 conversion and CH_4 selectivity remains the most promising approach for industrial application.

For the CO_2 methanation reaction, the eight proton-electron coupling transfer process ($CO_2 + 8\ H^+ + 8e^- \rightarrow CH_4 + 2\ H_2O$) limits its reaction rate [10]. Several strategies to facilitate this process through catalyst design and modification have been reported, including catalyst doping or morphological engineering to increase the oxygen vacancy concentration [11,12], adding basic oxides to increase the number of basic sites [13], or adding electron-based additives to modulate the internal electric field [14]. However, most of these strategies focus on improving CO_2 adsorption and activation, while the impact of post-activation reaction steps is not paid enough attention. The CO_2 methanation reaction involves several reaction steps generating multiple intermediates such as CO* , *CHO, $*CH_2O$, etc. [15]. The formation and conversion of these intermediates strongly affect the reaction rate of CO_2 methanation. In such complex tandem reactions, supported metal catalysts with a single specified active-site structure may not provide optimal catalytic reactivity for all steps of a multi-step reaction process, thus requiring new catalyst design strategies [16].

* Corresponding authors.
** Corresponding author at: Guangdong Provincial Key Laboratory of Materials and Technologies for Energy Conversion (MATEC), GTIIT, Guangdong 515063, China.
*** Corresponding author at: Institute of Process Engineering, Chinese Academy of Sciences, Beijing 100190, China.
E-mail addresses: fngu@ipe.ac.cn (F. Gu), wqxu@ipe.ac.cn (W. Xu), wxchen@bit.edu.cn (W. Chen), ziyi.zhong@gtiit.edu.cn (Z. Zhong), fbsu@ipe.ac.cn (F. Su).
[1] Tengfei Zhang and Peng Zheng contributed equally to this work.

https://doi.org/10.1016/j.apcatb.2022.122190
Received 22 September 2022; Received in revised form 12 November 2022; Accepted 15 November 2022
Available online 17 November 2022
0926-3373/© 2022 Elsevier B.V. All rights reserved.

Various low-cost Ni-based catalysts with Ni nanoparticles as active sites have been reported for CO and CO_2 methanation, including Ni/Al_2O_3 [17,18], Ni/SiO_2 [18,19], Ni/TiO_2 [20], Ni/CeO_2 [21], Ni/MgO [22], Ni/CNTs [23], and Ni/ZrO_2 [24]. Some reports have demonstrated that Ni-based catalysts are more active toward CO methanation than CO_2 methanation [25–27]. Therefore, reducing CO_2 to CO and then forming CH_4 on Ni sites may improve catalytic performance.

On the other hand, Ru-based catalysts also are efficient for CO_2 methanation [28–30], and the addition of low amounts of Ru to Ni catalysts reduces the Ni particle size and improves the reduction of NiO as well as the adsorption of H_2, thus lead to excellent catalytic performance for CO_2 methanation [31–33]. However, their high cost limits their practical application [34]. Improving metal utilization efficiency to reduce metal loading is an effective solution to this issue [35]. For example, the Ru single-atom catalysts (SACs) of Ru(SA)/CeO_2 showed a high CO_2 activation capacity, with a TOF_{CO2} of 4.59×10^{-3} s^{-1} at 190 °C, almost 8.7 times higher than the TOF_{CO2} of Ru(NP)/CeO_2 [36]. However, it was reported that Ru single atoms supported on Al_2O_3 and CeO_2 are highly selective for the reverse water gas shift (RWGS) due to a weaker binding to CO than Ru NPs, which is more favorable for CO desorption [37]. Therefore, adding Ru single atoms to Ni-based catalysts to form a dual active site tandem catalyst may improve the CO_2 methanation reaction rate.

Tandem catalysts have been applied to the photo-reduction and electro-reduction of CO_2 to CH_4 [38–41]. Li and co-authors presented a novel tandem electrocatalyst comprising a single-atom Ir_1-doped hybrid Cu_3N/Cu_2O multisite that efficiently converted CO_2 to CH_4 [8]. Zheng et al. constructed synergistic Pd_1 and Pd NPs on graphitic carbon nitride to realize a high selectivity of 97.8% with a yield of 20.3 μmol $g_{cat.}^{-1}$ h^{-1} for the photoreduction of CO_2 to CH_4 [42]. However, no research has been reported on thermal catalytic CO_2 methanation by tandem catalysts.

In this work, we successfully constructed a dual-functional site tandem catalyst with Ru single atoms and Ni nanoparticles, which are supported on CeO_2 nanorods (Ru_1Ni/CeO_2) for CO_2 methanation. It is noted that the preparation of this catalyst does not involve complicated synthesis procedures, toxic or expensive chemicals, and harsh treatment conditions. The abundant oxygen vacancies on the surface of CeO_2 nanorods and the high affinity of their surface lattice oxygen atoms are helpful for the formation and stabilization of single Ru atoms, especially under calcination and reducing atmospheres [43]. The Ru_1Ni/CeO_2 catalyst shows higher activity for CO_2 methanation than the Ru_1/CeO_2 and Ni/CeO_2 catalysts. This is because CO_2 dissociation to CO first occurred on Ru_1 active sites, and subsequently, CO were prone to desorb from Ru_1. Simultaneously, Ni with good CO affinity could further optimize the *CO to *CHO route to release CH_4. It thereby promotes the tandem pathways from the optimization of CO_2 dissociation to the thermodynamic limit of forming *CHO and achieves superior CO_2 methanation. In addition, density functional theory (DFT) calculations further revealed that the adjacent Ru_1 and Ni reduced the energy barrier for CO_2 to *CHO, thus making the CO_2 methanation reaction easier. Our work provides a new design strategy for catalyzing and accelerating CO_2 methanation.

2. Experimental section

2.1. Chemicals and materials

Nickel nitrate hexahydrate ($Ni(NO_3)_2{\cdot}6H_2O$) and cerium nitrate hexahydrate ($Ce(NO_3)_3{\cdot}6H_2O$) were purchased from Shanghai Aladdin Biochemical Technology Co., Ltd. Sodium hydroxide (NaOH), ethanol, and ruthenium chloride hydrate ($RuCl_3{\cdot}H_2O$) were purchased from Shanghai Macklin Biochemical Co., Ltd., China and all the chemicals used without further purification.

2.2. Synthesis of materials

2.2.1. Synthesis of CeO_2 material

Synthesis of CeO_2 nanorods: CeO_2 nanorods were prepared using a conventional hydrothermal method based on a previous report [43]. $Ce(NO_3)_3{\cdot}6H_2O$ (1.73 g) and NaOH (19.20 g) were dissolved in 10 mL and 70 mL of deionized water, respectively. The Ce^{3+} salt solution was dropped into the NaOH solution under vigorous stirring. After stirring for 30 min, the slurry was transferred to an autoclave and maintained at 100 °C for 24 h. The solid was separated by centrifugation, washed three times with deionized water, dried overnight at 50 °C, and calcined at 400 °C in air for 1 h (heating rate of 5 °C min^{-1}).

2.2.2. Synthesis of catalysts

Synthesis of Ru_1/CeO_2 nanorods: a mixture of $Ce(NO_3)_3{\cdot}6H_2O$ (1.73 g) and $RuCl_3{\cdot}H_2O$ (0.01 g), and NaOH (19.20 g) were dissolved in 10 mL and 70 mL of deionized water, respectively. The salt solution (Ru^{3+} and Ce^{3+}) was dropped into the NaOH solution under vigorous stirring. After being stirred for 30 min, the slurry was transferred to an autoclave and maintained at 100 °C for 24 h. The solid was separated by centrifugation, washed three times with deionized water, dried overnight at 50 °C, and calcined at 400 °C in air for 1 h (heating rate of 5 °C min^{-1}) followed by reduction at 400 °C in pure H_2 for 1 h (heating rate of 5 °C min^{-1}, H_2 flowing rate of 100 mL min^{-1}). This catalyst was denoted Ru_1/CeO_2 with a Ru loading of 0.91 wt% determined by inductively coupled plasma optical emission spectroscopy (ICP-OES).

Synthesis of 5 wt% Ni/CeO_2 and 5 wt% $NiRu_1/CeO_2$: $Ni(NO_3)_2{\cdot}6H_2O$ (0.08 g) was dissolved into 50 mL of ethanol, then CeO_2 or Ru_1/CeO_2 powder (3.00 g) was added to the above solution. The mixture was stirred at 50 °C until ethanol evaporated and then calcined at 400 °C for 1 h after dried at 50 °C overnight. These catalysts were denoted Ni/CeO_2 and Ru_1Ni/CeO_2. The mixture was stirred at 50 °C until the ethanol evaporated, then calcined at 400 °C for 1 h, followed by reduction at 400 °C in pure H_2 for 1 h (heating rate of 5 °C min^{-1}, H_2 flowing rate of 100 mL min^{-1}).

Synthesis of the Ru_1/CeO_2 +Ni/CeO_2 mixed catalyst: above obtained Ni/CeO_2 (0.10 g) and Ru_1/CeO_2 (0.10 g) were mixed well with a mortar and pestle.

2.3. Characterization

N_2 adsorption/desorption isotherms were measured using a surface area and pore size analyzer (Quantachrome, NOVA 3200e). The specific surface area was determined according to the Brunauer–Emmett–Teller (BET) method in the relative pressure range of 0.05 − 0.20. The samples were degassed at 300 °C for 4 h and analyzed at −196 °C. X-ray diffraction (XRD) patterns were measured on a PANalytical X'Pert PRO MPD using Cu K_α radiation (λ = 1.5418 Å) at 40 kV and 40 mA, and compared with the standard XRD patterns in the database of the Joint Committee on Powder Diffraction Standards (JCPDS). The crystal size of the sample was calculated using the Debye-Scherrer equation. Bright-field transmission electron microscopy (BF-TEM) images were measured using a JEM-2010 F transmission electron microscope (JEOL, Japan) under a working voltage of 200 kV. Thermogravimetric (TG) analysis was conducted on a Seiko Instruments EXSTAR TG/DTA 6300. 10 mg of the sample was used and heated under air (200 mL min^{-1}) from room temperature up to 900 °C (10 °C min^{-1}). The aberration-corrected (AC) HAADF-STEM images were obtained on aberration-corrected high-angle annular dark-field scanning transmission electron microscopy (FEI-Titan Cubed Themis G2 300, Netherlands). The extended X-ray absorption spectroscopy (XAS) measurements at lower potentials at BL14W1 were carried out at the Shanghai Synchrotron Radiation Facility (SSRF). XAS data were analyzed using the IFEFFIT package, in which energy calibration to respective metal foils and spectral normalization were performed using Athena software [44]. X-ray photoelectron spectroscopy (XPS) spectra were recorded using a Kratos Axis Ultra

spectrometer employing nonmonochromatized Al Kα radiation (1486.6 eV) operated at 15 kV and 20 mA under pressure below 10^{-9} Pa to analyze the valence of each element. H_2 temperature-programmed reduction (H_2-TPR) and H_2 temperature-programmed desorption (H_2-TPD) experiments were carried out on a Quanta chrome Automated chemisorption analyzer (chemBET pulsar TPR/TPD). For H_2-TPR, a 0.05 g sample was loaded in a quartz U-tube, heated from room temperature to 200 °C at 10 °C min^{-1} and maintained for 1 h under He flow. Then, the sample was cooled to room temperature and heated to 800 °C at 10 °C min^{-1} under binary gas (10.0 vol% H_2/Ar) with a gas flow of 30 mL min^{-1}. For H_2-TPD, 0.05 g catalyst was used and reduced in situ at 400 °C for 1 h by H_2/Ar flow. Then, the sample was cooled to room temperature and saturated with H_2. After removing the physically adsorbed H_2 by purging with Ar for 2 h, the sample was heated to 600 °C with a ramping rate of 10 °C min^{-1} in an Ar flow (30 mL min^{-1}). The consumed or desorbed H_2 was detected continuously as a function of the increasing temperature using a thermal conductivity detector (TCD).

Raman spectra were recorded from 100 to 1500 cm^{-1} on a Renishaw inVia Raman spectrometer with an excitation wavelength of 532 nm and laser power of 5 mW.

Fourier transform infrared spectra (FT-IR) were taken on a Tensor 27 spectrometer (Bruker). In situ diffuse reflectance infrared Fourier transform spectroscopy (In situ DRIFTS) experiments were performed to detect the intermediate species adsorbed on the catalyst in the CO_2 methanation reaction. In situ DRIFTS spectra were continuously collected using a Nicolet IS50 spectrometer equipped with an MCT detector cooled by liquid nitrogen. Before the test, the catalyst was first reduced in H_2 flow (60 mL min^{-1}) at 400 °C for 1 h. Then, 10 mg of the reduced sample [m (catalyst): m(KBr) = 1:10] was placed on the sample holder at the center of the cell. The test conditions were the atmosphere of the simulated real reaction process. Then, an H_2/CO_2 (molar ratio of 4) mixture was introduced and heated to 400 °C at a heating rate of 10 °C min^{-1}. The spectra were collected by recording each scan every 7 s from 600 to 4000 cm^{-1} with a resolution of 0.9 cm^{-1}.

2.4. Catalytic measurement

The catalytic activity test was carried out in a fixed bed reactor equipped with a quartz tube (I.D. 8 mm) at 0.1 MPa, in which the thermocouple was inserted into the furnace chamber to control the reaction temperature. Additionally, to avoid the influence of heat transfer, the catalyst (catalyst diluted with quartz sand with a length of ca. 6 cm) was placed in the flat-temperature zone (ca. 10 cm) of the furnace, and the addition of the quartz sand was to avoid the generation of hotspots in the catalyst bed. Moreover, another thermocouple was inserted into the catalyst bed with a casing pipe to measure its temperature. These measures were combined to eliminate the influences of mass and heat transfers in the catalytic tests. For the activity test, typically, 0.1 g catalyst (20−40 mesh) diluted with 5.0 g quartz sand (20−40 mesh) was uploaded to a quartz tube with a height of ca. 6 cm, and the gas flow rate was 50 mL min^{-1}, corresponding to a weight hourly space velocity of 30000 mL g^{-1} h^{-1}. First, the catalyst was reduced at 400 °C in pure H_2 (100 mL min^{-1}) for 1 h and then cooled to the starting reaction temperature in H_2. Then, the mixed CO_2 and H_2, as well as N_2 (as an internal standard), were introduced into the reactor at a molar ratio of $CO_2/H_2/N_2$ = 9/36/5 (50 mL min^{-1} to investigate the catalytic activity of catalysts at 225−400 °C. The temperature-programmed heating rate was 5 °C min^{-1} in the total temperature range, and to obtain a steady state result at each temperature point before the product analysis, the reaction temperature was maintained for 1 h. Both the inlet and outlet gases were analyzed online by a Micro GC 3000 A (Fusion, INFICON) equipped with a TCD. In addition, a 100 h lifetime test of CO_2 methanation was performed at 300 °C, 0.1 MPa, and 30000 mL g^{-1} h^{-1}. The CO_2 conversion, CH_4 selectivity, and CH_4 yield are defined as follows [45]:

$$\mathrm{CO_2 conversion}: X_{CO_2} = \frac{V_{CO_2,in} - V_{CO_2,out}}{V_{CO_2,in}} \times 100\% \quad (1)$$

$$\mathrm{CH_4 selectivity}: S_{CH_4} = \frac{V_{CH_4,out}}{V_{CO_2,in} - V_{CO_2,out}} \times 100\% \quad (2)$$

$$\mathrm{CH_4 yield}: Y_{CH_4} = \frac{V_{CH_4,out}}{V_{CO_2,in}} \times 100\% \quad (3)$$

where X is the conversion of CO_2, S is the selectivity of CH_4, Y is the CH_4 yield, $V_{CO2,in}$ and $V_{CO2,out}$ are the volume flow rates of CO_2 at the inlet and outlet of the reactor at standard temperature and pressure (STP), mL min^{-1}.

The normalized reaction rate and activation energy for CO_2 methanation over the catalysts were measured at 0.1 MPa with a catalyst loading of 0.1 g (20−40 mesh) diluted with 5.0 g quartz sand (20−40 mesh). The experiments were performed at different total gas flow rates of 25, 50, and 100 mL min^{-1} at 200, 210, 220, and 230 °C to maintain CO_2 conversion in the 2–20% range. The activation energy was calculated using the Arrhenius equation. The activity was determined using the following equation [45]:

$$Activity = \frac{X_{CO_2} \times M_{CO_2,in}}{m_{cat} \times \omega_{metal} \times \Delta_t} \quad (4)$$

where X_{CO2} is the conversion of CO_2, M_{CO2} in represents the moles of CO_2 at the inlet, and ω_{metal} is the metal loading, as well as $m_{cat.}$ is the mass of catalyst.

2.5. Computational detail

All the density functional theory (DFT) calculations were performed through the Vienna ab initio simulation package (VASP) [46,47]. The core electrons were treated with the projector augmented-wave (PAW) pseudopotentials. The exchange-correlation function was described by generalized gradient approximation (GGA) using Perdew-Burke-Ernzerhof (PBE) function[48]. The van der Waals interactions were corrected by the DFT-D3 method [49]. The plane-wave cutoff energy was set as 450 eV, the Monkhorst-Pack k-point was set as 2 × 2 × 1, and the U_{eff} = 5.0 eV was applied to the Ce 4 f states [50]. The convergence criterion for the geometric relaxation was 0.02 eV/Å. The transition states for all the elementary reactions were searched using the CI-NEB method [51]. The adsorption energy was calculated using the following equation: $E_{ads} = E_{gas/surf} - (E_{gas} + E_{surf})$. The $E_{gas/surf}$ represents the energy of the whole adsorbed system, E_{gas} represents the energy of a free molecule in the gas phase, and E_{surf} represents the energy of an independent catalyst surface. The reaction barrier was calculated using the subsequent equation: $E_a = E_{TS} - E_r$. The E_{TS} and E_r represent the energies of transition states and reactants, respectively.

The model of the Ni10 cluster was built based on previous research [52]. The CeO_2 (111) was modeled using a (4 × 4) supercell containing four atomic layers. And the atoms in the bottom two layers were fixed, while the rest of the atoms were relaxed. The vacuum region was set as 15 Å. Afterwards, the Ru single atom or Ni10 cluster was loaded on the CeO_2 (111) surface, as shown in Fig. S1.

3. Results and discussion

3.1. Characterization of the catalysts

3.1.1. XRD, BET, H_2-TPR, and H_2-TPD analysis

Rod-like CeO_2 support and Ru_1/CeO_2 catalyst were prepared via a hydrothermal method. Ru_1Ni/CeO_2 and Ni/CeO_2 catalysts were further prepared by the impregnation method followed by H_2 reduction using Ru_1/CeO_2 and Rod-like CeO_2 as supports, respectively. In Fig. 1a, the XRD peaks observed for the catalysts and CeO_2 support with 2θ of 28.54,

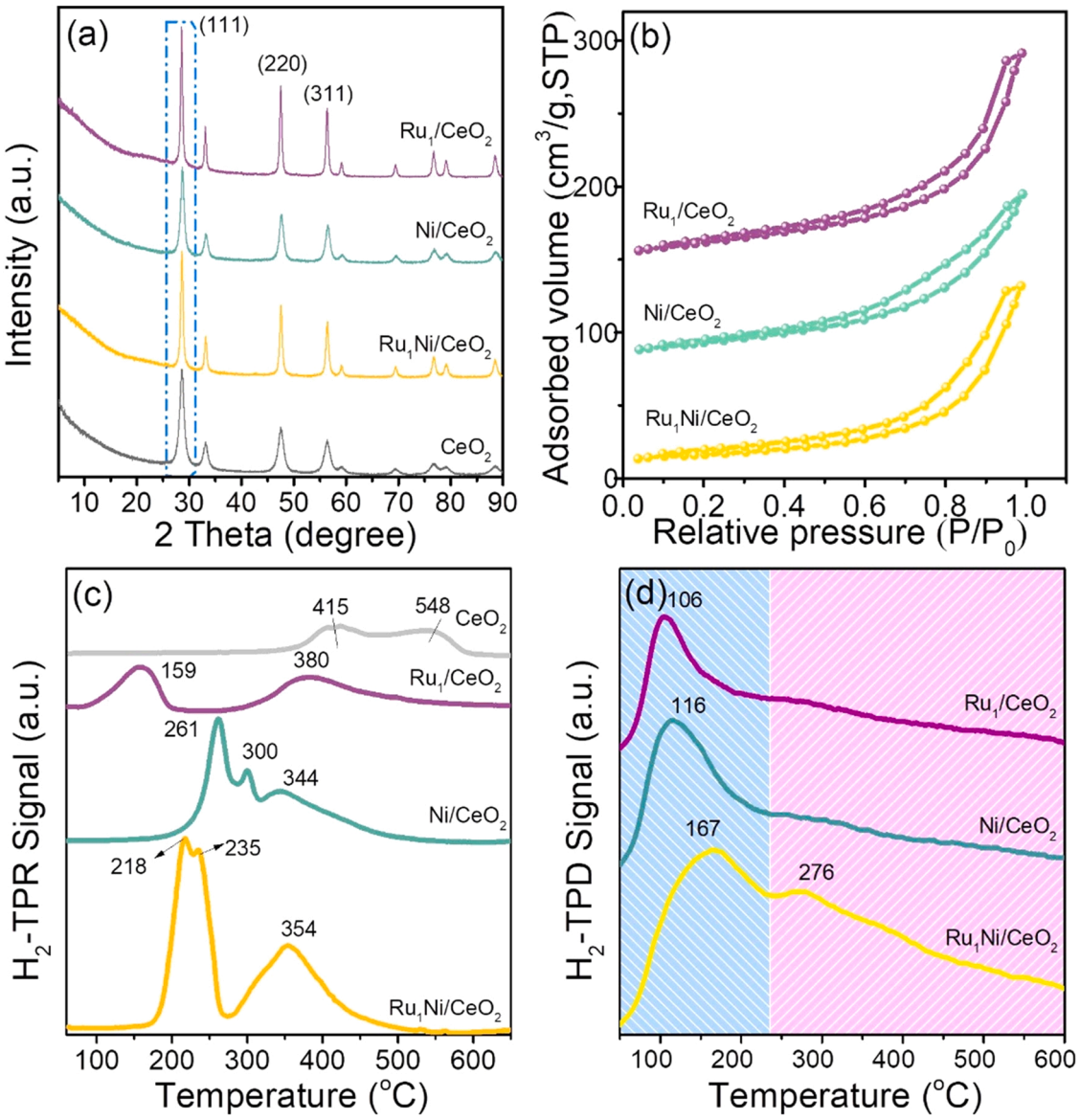

Fig. 1. (a) XRD patterns, (b) N_2 adsorption-desorption isotherms, (c) H_2-TPR, and (d) H_2-TPD profiles of all the catalysts.

47.52, and 56.38°are indexed to the (111), (220), and (311) planes of CeO_2 with the typical fluorite structure (JCPDS 43–1002) [53]. No characteristic diffraction peaks belonging to Ni and Ru could be detected due to their low loadings or small nanocrystals. Ru_1/CeO_2, Ni/CeO_2, and Ru_1Ni/CeO_2 exhibit type IV N_2 adsorption isotherms with an H3-type hysteresis loop (Fig. 1b) and similar surface area and pore volume (Table 1).

Table 1
Physiochemical properties of the all catalysts.

Samples	S_{BET}[a] ($m^2\ g^{-1}$)	V_p[b] ($cm^3\ g^{-1}$)	H_2 uptake[c] (μmol g^{-1})	O_{ads}/(O_{ads} + O_{latt}) molar ratio (%)	Ce^{3+}/(Ce^{3+} + Ce^{4+}) molar ratio (%)	I_D/I_{F2g} ratio (%)
Ru_1/CeO_2	72.6	0.23	155.8	39.4	15.4	10.7
Ni/CeO_2	71.1	0.19	174.8	41.1	18.5	39.1
Ru_1Ni/CeO_2	67.9	0.20	355.0	57.7	22.3	44.8

[a] Surface area, derived from BET equation.
[b] Pore volume, obtained from the volume of nitrogen adsorbed at the relative pressure of 0.99.
[c] H_2 uptake, calculated based on the H_2-TPD results.

Fig. 1c shows the H_2-TPR profiles of all the catalysts and CeO_2 support. For the CeO_2 support, two reduction peaks are observed at about 415 and 548 °C, ascribed to the release of surface and subsurface oxygen on CeO_2 through reducing the associated Ce^{4+} to Ce^{3+} [54]. For Ru_1/CeO_2, the new peak at ~159 °C can be assigned to remove the reactive surface oxygen on CeO_2 and RuO_x to metallic Ru [36]. In addition, the peak at 380 °C due to the reduction of Ce^{4+} is significantly lower than the reduction temperature of normal CeO_2, probably caused by the H-spillover effect [36]. For Ni/CeO_2, three main peaks at 261 °C, 300 °C, and around 344 °C are observed, attributed to the NiO species with weak, moderate, and strong interactions with the CeO_2 support [55], respectively. For Ru_1Ni/CeO_2, the observed peaks at 218 °C and 235 °C are attributed to the reduction of the RuO_x species to metallic Ru and NiO species to metallic Ni, respectively. In contrast, the peak at 354 °C is attributed to the reduction of Ce^{4+} to Ce^{3+} associated with the surface oxygen species. The reduction temperature of RuO_x to metallic Ru is gradually increased from 159 °C in Ru_1/CeO_2 to 218 °C in Ru_1Ni/CeO_2 due to the twice calcination of the latter at 400 °C, which increased the interactions between Ru and CeO_2. Compared with the

peak at 261 °C in Ni/CeO_2, this reduction peak of Ru_1Ni/CeO_2 shifts to 235 °C, indicating that adding Ru_1 species can improve the reducibility of the NiO species through hydrogen dissociation and the spill-over mechanism [56]. Ru_1Ni/CeO_2 has a more substantial peak at 350 °C than Ni/CeO_2, indicating the former has more oxygen vacancies [11], or more Ce^{4+} can be reduced to Ce^{3+} than the latter. The results will be further discussed in the XPS and Raman characterization sections. Fig. 1d shows the H_2-TPD profiles of all the catalysts. The low-temperature desorption peaks at around 50–240 °C are attributed to the hydrogen adsorbed on the active metal species. The broad peaks from 240 to 600 °C are adsorbed hydrogen on the CeO_2 supports. Probably part of them was spilled over from the active metal sites to the support [36]. Among all the catalysts, Ru_1Ni/CeO_2 shows the highest H_2 uptake of 355.0 μmol g^{-1} (Table 1), indicating that the simultaneous presence of Ni particles and Ru single atoms could slightly improve the chemisorption capacity of H_2.

3.1.2. XPS and Raman analysis

The O 1 s spectra are deconvoluted into two peaks, as shown in Fig. 2a. The main peak at ~528.76 eV can be assigned to lattice oxygen (O_{latt}), while that at ~530.80 eV is attributed to surface-adsorbed oxygen (O_{ads}).[57] The surface $O_{ads}/(O_{ads} + O_{latt})$ molar ratios are also calculated and summarized in Table 1 through quantitative analyses of the O 1 s XPS spectra. The $O_{ads}/(O_{ads} + O_{latt})$) ratio is 39.4% for Ru_1/CeO_2, 41.1% for Ni/CeO_2, and 57.7% for Ru_1Ni/CeO_2, suggesting that Ru_1Ni/CeO_2 has more oxygen vacancies and, thus, more active adsorbed oxygen species. For the complex Ce 3d XPS spectra, each one is numerically deconvoluted into eight components (Fig. 2b). The six peaks at 881.94, 888.13, 897.72, 898.30, 900.36, 906.97, and 916.15 eV are assigned to surface Ce^{4+}, and the other two peaks at 884.00 and 901.93 eV to surface Ce^{3+} [58]. The calculated ratios of the $Ce^{3+}/(Ce^{3+} + Ce^{4+})$ are compiled in Table 1 and show the order of $Ru_1/CeO_2 < Ni/CeO_2 < Ru_1Ni/CeO_2$. More Ce^{4+} ions were reduced in Ru_1Ni/CeO_2 due to the H-spillover effect, which correlates well with the surface-absorbed oxygen concentration in the materials. For Ni/CeO_2, the strong peaks at around 855.56 and 861.61 eV are related to the Ni^{2+} species, while the peak at 853.68 is assigned to Ni^0 (Fig. 2c) [59]. The above peaks shift to low values of 854.83, 860.47, and 853.16 eV, respectively, in the spectrum of Ru_1Ni/CeO_2, which can be attributed to the higher electron-withdrawing capacity of Ni-Ru_1 dual-sites compared to the single-Ni sites of Ni/CeO_2, thus resulting in an increased electron density on the Ni sites. For the XPS of Ru 3d (Fig. S2), unfortunately, the

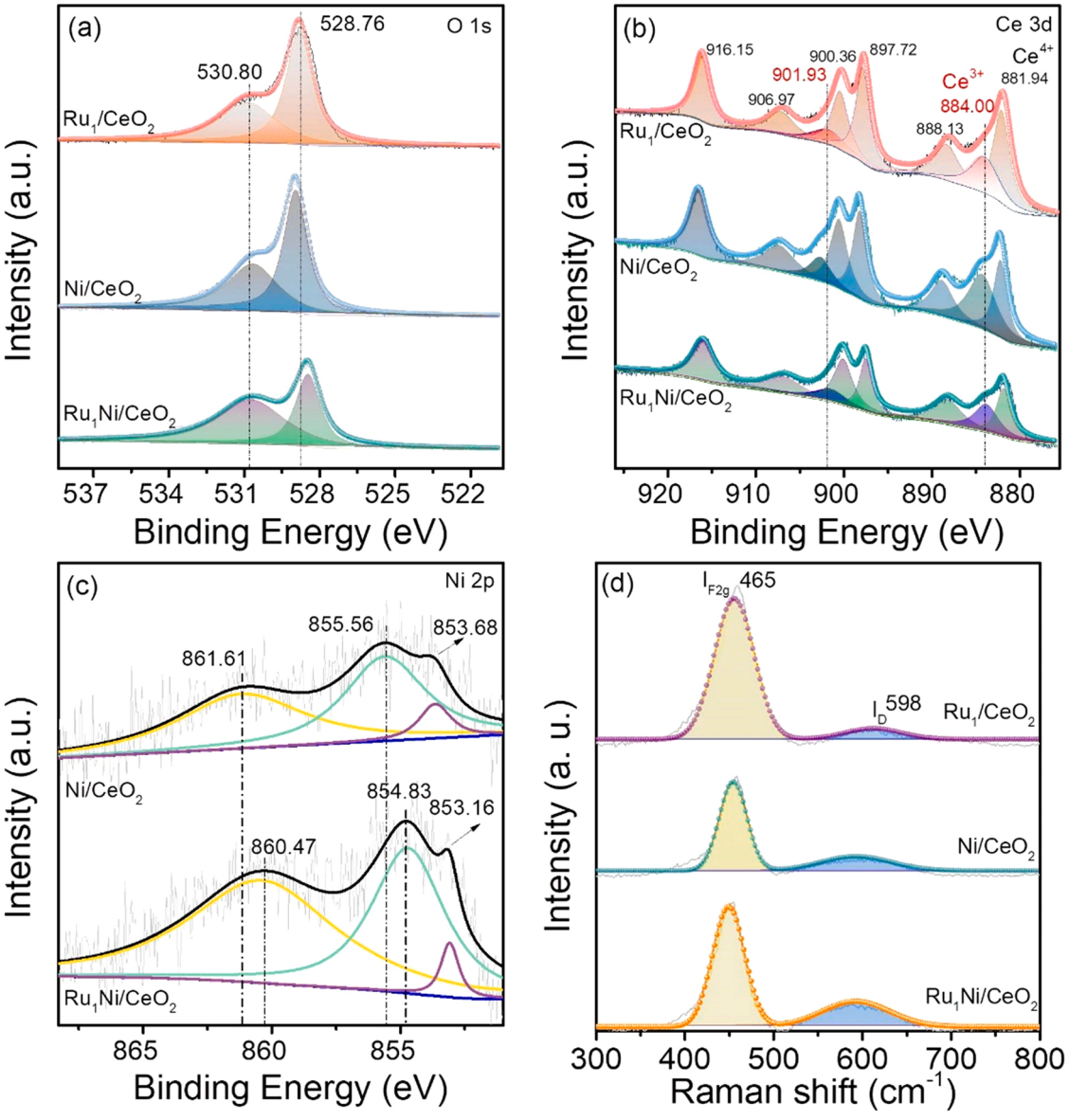

Fig. 2. XPS spectra: (a) O 1s, (b) Ce 3d, (c) Ni 2p, and (d) Raman spectra of all the catalysts.

signal was too weak to be detected, and also, there is an overlap between the C 1 s and Ru 3d peaks in the spectra of Ru_1/CeO_2 and Ru_1Ni/CeO_2, so the XPS peaks of Ru 3d could not be deconvoluted to analyze the Ru species in different oxidation states [11]. For the Raman signal of the catalysts, defective sites in the lattice lead to a D mode at 598 cm^{-1}, which represents a Frenkel-type oxygen vacancy resulting from the transfer of the oxygen anion from a tetrahedral site to an octahedral site, and an intrinsic F_{2g} mode at 465 cm^{-1} (Fig. 2d) [60,61]. Moreover, the oxygen vacancies revealed in the Raman spectrum are generated via repositioning oxygen ions, which are hardly affected by O_2 molecules at room temperature, so the content of oxygen vacancies can be more accurately calculated. Thus, the intensity ratios of I_D/I_{F2g} were calculated to reflect the concentration of oxygen vacancies (Table 1). I_D/I_{F2g} is 10.7% for Ru_1/CeO_2, 39.1% for Ni/CeO_2, and 44.8% for Ru_1Ni/CeO_2. Ru_1Ni/CeO_2 has the highest oxygen vacancy content, consistent with the XPS results. Previous studies have shown that surface oxygen vacancies can prevent the aggregation of Ru single atoms and are actively involved in the CO_2 methanation process [53,62].

3.1.3. TEM observation and XAS analysis

Fig. 3 shows AC HAADF-STEM images of Ru_1/CeO_2 and Ru_1Ni/CeO_2. Fig. 3a shows the presence of a clear lattice fringe with a spacing of 0.31 nm, which is indexed to the (111) plane of CeO_2 with high crystallinity [59]. Moreover, many bright dots attributed to Ru atoms are dispersed on the surface of CeO_2 (Fig. 3a and S3). For Ru_1Ni/CeO_2, the two-dimensional lattice fringe can be readily identified in Fig. 3b. The interplanar distances of 0.28 and 0.31 nm correspond to the CeO_2 (200) and (111) planes, respectively, and 0.20 nm belongs to Ni (111) [59]. The HAADF-STEM image in Fig. 3c shows that many Ru atoms and Ni nanoparticles are dispersed on the surface of CeO_2 nanorods. In addition, the corresponding EDX spectroscopy elemental mapping images show that there is no significant overlap between Ru and Ni (Fig. 3d—3d_2) and both of them are homogeneously dispersed on Ce (Fig. d_3) and O (Fig. d_4), indicating that Ru and Ni do not form alloy structures but present separately. Figs. 3e and 3f show the results of the extended X-ray absorption fine structure (EXAFS) spectroscopy for all the catalysts. For Ru_1/CeO_2 and Ru_1Ni/CeO_2, the most noticeable scattering is observed at 1.5 Å, ascribed to the coordination shell of

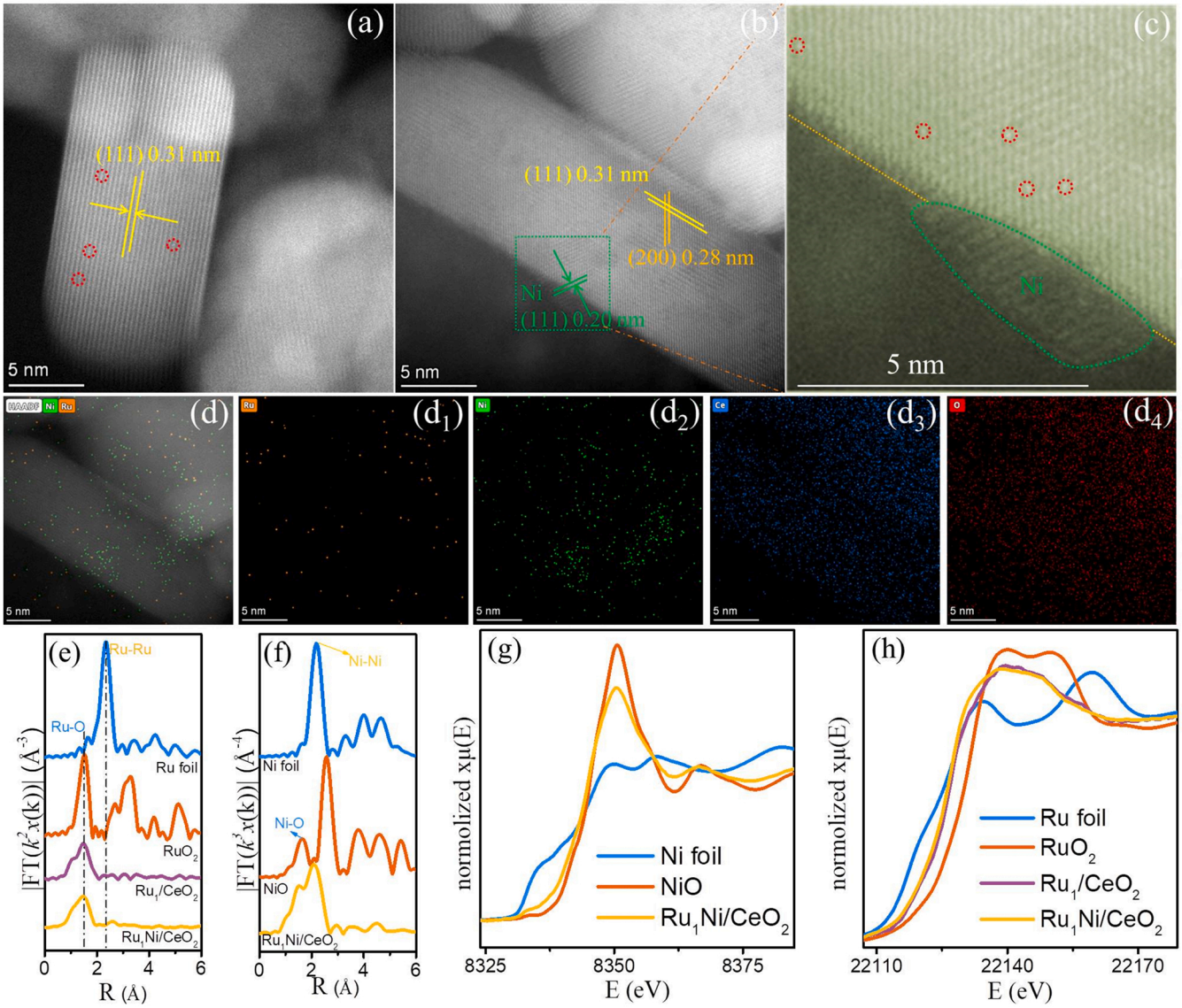

Fig. 3. AC-HAADF-STEM image of Ru_1/CeO_2 (a) and Ru_1Ni/CeO_2 (b), enlarged view (c) of the region marked with green box in (b), element EDX mapping layered image (d) and corresponding mapping images of Ru (d_1), Ni (d_2), Ce (d_3), and O (d_4) for Ru_1Ni/CeO_2. Fourier transforms magnitude of EXAFS spectra: (e) k^2-weighted Ru K-edge for Ru_1/CeO_2 and Ru_1Ni/CeO_2, and (f) k^3-weighted Ni K-edge for Ru_1Ni/CeO_2; and XANES profiles: (g) Ni K-edge for Ru_1Ni/CeO_2 and (h) Ru K-edge for Ru_1/CeO_2 and Ru_1Ni/CeO_2.

Ru−O. Their measured average coordination number (CN) of Ru-O for the two samples is 3.7 and 3.4 (Table S1), respectively. The Ru K-edge does not support the existence of the Ru−Ru structure, confirming the dominant isolated nature of the Ru species. These Ru atoms in Ru_1/CeO_2 and Ru_1Ni/CeO_2 should be available for chemical adsorption and subsequent reactions. For Ru_1Ni/CeO_2, in addition to the relatively weak peak at 1.5 Å assigned to Ni−O, a major peak at 2.1 Å that corresponds to the Ni−Ni coordination shell could be observed, indicating the presence of relatively large Ni nanoparticles (with a Ni−O CN of 2.4 and a Ni−Ni CN of 10.5) (Table S1), which is in good agreement with the AC-HADDF-STEM result. The X-ray absorption near edge structure (XANES) features of Ru_1Ni/CeO_2 falls between Ni foil and NiO (Fig. 3g). Moreover, the Ni adsorption edge of Ru_1Ni/CeO_2 is close to that of NiO. This indicates that the Ni species has a charge transfer to the CeO_2 and are in cationic states. In the Ru K-edge XANES profiles (Fig. 3h), the absorption edge position of Ru_1/CeO_2 and Ru_1Ni/CeO_2 were located between the Ru foil and RuO_2, showing the moderate average oxidation state of Ru.

3.2. Catalytic performance of catalysts

The CO_2 methanation catalytic performances of Ru_1/CeO_2, Ni/CeO_2, and Ru_1Ni/CeO_2 were investigated under 0.1 MPa and a high WHSV of 30000 mL g^{-1} h^{-1} (Fig. 4). Overall, the CO_2 conversion on Ru_1Ni/CeO_2 is obviously higher than that on Ru_1/CeO_2 and Ni/CeO_2, especially at low temperatures (225−325 °C), suggesting a tandem effect of Ru atoms and Ni particles on CO_2 methanation (Fig. 4a). Compared to Ni/CeO_2 and Ru_1Ni/CeO_2, Ru_1/CeO_2 exhibits a lower selectivity of approximately 30% for producing CH_4 and higher selectivity of ~70% for producing CO (Figs. 4b and 4c). Notably, the product distribution remained almost unchanged throughout the temperature interval (225−400 °C), indicating that the Ru_1 site can only catalyze the conversion of CO_2 to CO. This is due to the weaker binding of CO on the Ru_1 site, which is more favorable for CO desorption. In addition, the CO_2 conversion, CH_4 selectivity, and CO selectivity on Ru_1/CeO_2 +Ni/CeO_2 are almost the same as those on Ni/CeO_2, and the CO_2 conversion is much lower than that on Ru_1Ni/CeO_2, indicating that CO generated on Ru_1/CeO_2 was hydrogenated to CH_4 on Ni/CeO_2, but its catalytic efficiency is lower than that of Ru_1Ni/CeO_2. Furthermore, Ru_1Ni/CeO_2 shows a higher CO_2 conversion than the Ru or Ni-based catalysts reported in the literature (Table S2) [57,63–67], even though a much higher space velocity in this work was used. Furthermore, the Ru_1Ni/CeO_2 shows the highest activity of 7.32 $mol_{CO2}{\cdot}g^{-1}$ h^{-1} (Table S2), which is 7.6 times of the reported 10Ni–Ru–(CaO–Al_2O_3) [67] and 3 ~ 14 times of the reported Ni/CeO_2 catalysts [57,63,66]. The activation energies of CO_2 methanation on different catalysts were measured. The Arrhenius plots show that the activation energy has the order of Ru_1Ni/CeO_2 (52.54 kJ mol^{-1}) > Ru_1/CeO_2 (58.03 kJ mol^{-1}) > Ni/CeO_2 (79.64 kJ mol^{-1}), which is highly consistent with the trend of CO_2 methanation activity at atmospheric pressure (Fig. 4d). Interestingly for Ru_1Ni/CeO_2 and Ru_1/CeO_2, the similar activation energy suggests that the same reaction mechanism may occur for CO_2 activation on both catalysts. In contrast, Ni/CeO_2 shows a high activation energy, indicating a different CO_2 activation mechanism. In addition, Ru_1Ni/CeO_2 and Ru_1/CeO_2 have similar apparent activation energies, suggesting that the same reaction mechanism may occur for CO_2 activation by both catalysts.

The performance and structural stability of the catalyst are critical to the catalyst. Regarding the catalytic stability, Ru_1Ni/CeO_2 showed > 99% selectivity for CH_4 and only a < 5% CO_2 conversion loss after a 100 h reaction at 300 °C (Fig. 4e). Probably, the 5% CO_2 conversion loss is caused by the aggregation of a small number of tiny Ni particles that have weak interactions with CeO_2. In addition, no XRD diffraction peaks

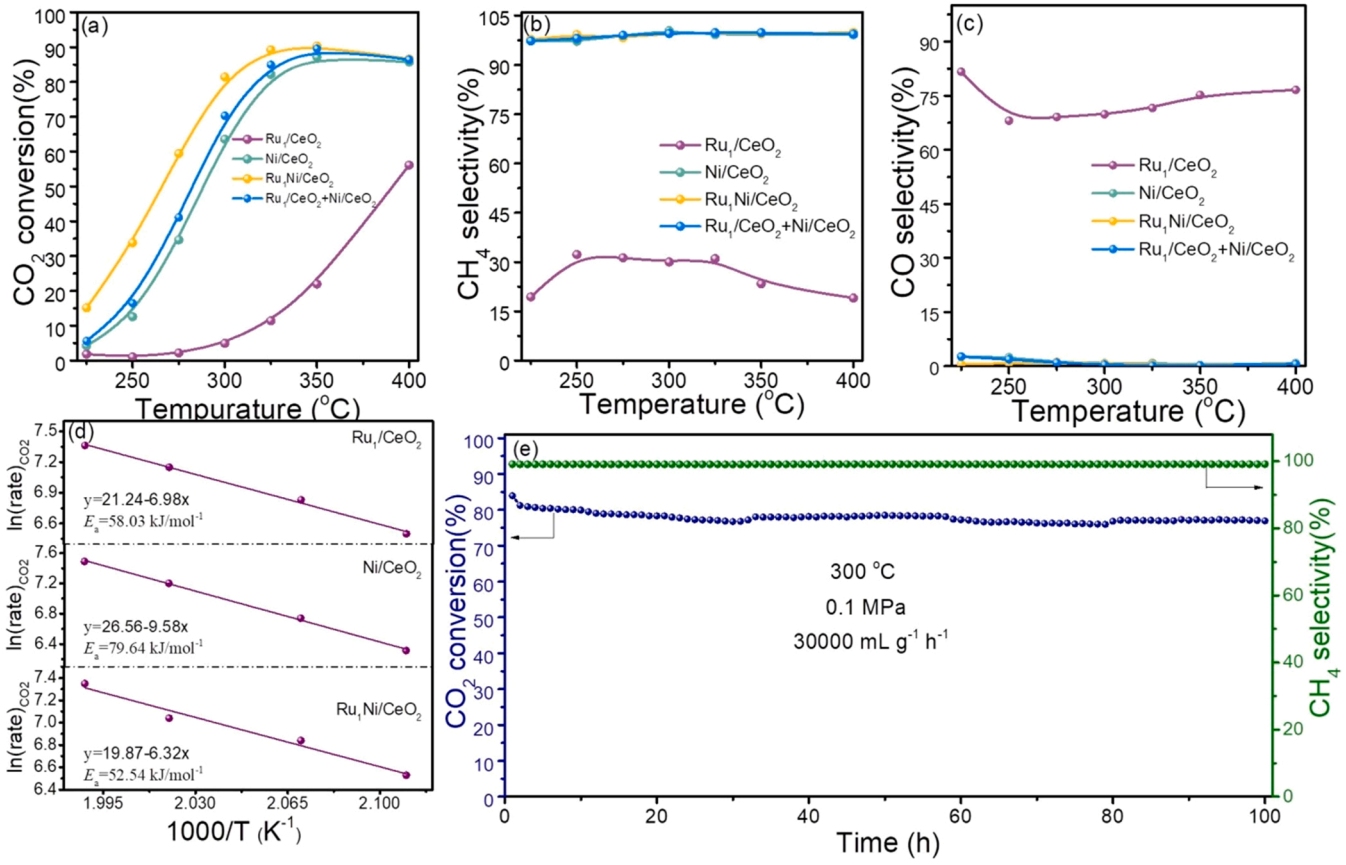

Fig. 4. Catalytic performance of all the catalysts: (a) CO_2 conversion, (b) CH_4 selectivity, (c) CO selectivity, and (d) Arrhenius plot; and (e) lifetime test of Ru_1Ni/CeO_2 at 300 °C.

of Ni and Ru in Ru_1Ni/CeO_2 were detected after the long-term stability test (Fig. S4), indicating that this catalyst had good stability. The measured high-resolution transmission electron microscope (HRTEM) images of Ru_1Ni/CeO_2 after the long-term test show that the Ni nanoparticle sizes are 3 − 4 nm (Fig. S5a), similar to that of the fresh catalyst (Fig. 3b). The EDX element mappings further validate that Ru and Ni are uniformly distributed on the CeO_x support without aggregation (Fig. S5b-S5i). In addition, the measured AC-HAADF-STEM images show that the Ru still maintains the single-atom dispersion state in Ru_1Ni/CeO_2 after the lifetime test (Fig. S6). The amount of carbon deposition on the spent catalyst after the long-term test was further measured by TG analysis, and the results are presented in Fig. S7. The weight loss curves can be divided into two parts. The first weight loss process that occurred below 200 °C belongs to the removal of the physically adsorbed water; while the second weight loss process between 200 and 330 °C is attributed to the release of CO_2, derived from the decomposition of CO_3^{2-} ions and the removal of hydroxyl groups [10]. The weight increase observed at 330–350 °C is attributed to the oxidation of Ni^0 [68], and no further weight loss is observed between 350 and 800 °C, indicating almost no carbon deposition on the spent catalyst.

3.3. Catalytic mechanism

3.3.1. In situ DRIFTS analysis

Figs. 5a-5c show the in situ diffuse reflectance infrared Fourier transform spectroscopy (In situ DRIFTS) spectra of the three catalysts measured in the reaction gas ($18\%CO_2/72\%H_2/N_2$) and the temperature range from 50 to 350 °C. For Ni/CeO_2 (Fig. 5a), the surface species of bicarbonates (1640 cm^{-1}), polydentate carbonates (1428 cm^{-1}), and monodentate carbonates (1509 cm^{-1}) were observed at different temperatures, and these peak intensities increased with temperature [69]. At temperatures above 200 °C, the bands of CO* (2022 and 1902 cm^{-1}), *CHO (1746 cm^{-1}), and CH_4 (3016 cm^{-1}) appeared [70–72]. Simultaneously, the bands of HCOO* (2842 and 1349 cm^{-1}) and carboxylate (1270 cm^{-1}) gradually decreased [73,74], indicating that CO* , *CHO, and CH_4 were mainly produced by HCOO* hydrogenation. In other words, the HCOO* reaction pathway for CO_2 methanation did occur on Ni/CeO_2. In addition, when the gas was changed to H_2 at 350 °C, bicarbonates gradually decreased due to quick conversion to HCOO* . *CHO, HCOO* , and also, carboxylate gradually disappeared (Fig. 5b). Thus, these intermediates are active species. On Ru_1/CeO_2 (Fig. 5c), the

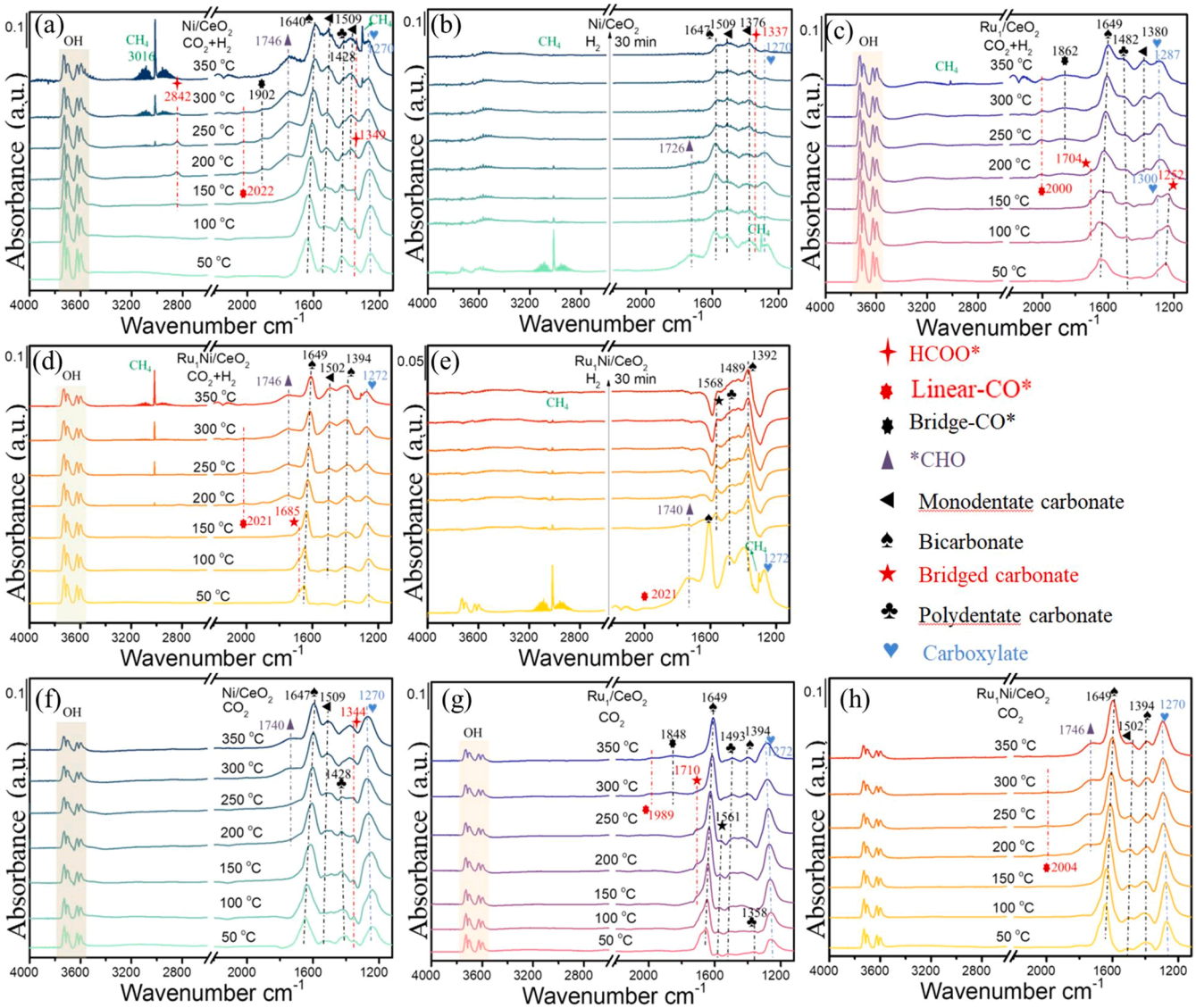

Fig. 5. In situ DRIFTS results on Ni/CeO_2 by introducing continuous flow of reaction gas 36% H_2/9% CO_2/Ar (a) and switching to gas 10% H_2/Ar (b); In situ DRIFTS results of CO_2 hydrogenation on Ru_1/CeO_2 (c) and Ru_1Ni/CeO_2 (d), and switching to gas 10% H_2/Ar on Ru_1Ni/CeO_2 (e); In situ DRIFTS results measured within the inlet gas 1% CO_2/He: Ni/CeO_2 (f), Ru_1/CeO_2 (g), and Ru_1Ni/CeO_2 (h).

typical adsorption species of CO_2 during methanation were bicarbonate (1394 cm^{-1}), monodentate (1380 cm^{-1}), carboxylate (1287 and 1300 cm^{-1}), and polydentate carbonates (1482 cm^{-1}). The two bands at 1704 and 1252 cm^{-1}, assigned to the bridged carbonates, disappeared at 200 °C. At the same time, the bands of linear-CO* (2000 cm^{-1}) [75] and bridge-CO* (1704 cm^{-1}) [71] appeared and did not significantly change with increasing temperature. A weak band of CH_4 at 3016 cm^{-1} could not be observed until 350 °C. The above results indicate that CO_2 can be rapidly converted to CO* on Ru_1/CeO_2, but the weak binding of CO* to Ru prevents further hydrogenation; thus, the gas phase CO is the final product. In short, the CO pathway for CO_2 methanation occurs on Ru_1/CeO_2, and the direct CO_2 dissociation forms CO* . For Ru_1Ni/CeO_2, the bands of CO* , *CHO, and CH_4 appeared from 200 °C, and the band of CO* reached the maximum intensity at 250 °C, then it decreased. In addition, the intensities of the CH_4 bands were much stronger than those for the Ru_1/CeO_2 catalyst, indicating that the catalyst with the Ni sites can further transform CO* into CH_4. The reaction pathways of CO_2 methanation over Ru_1Ni/CeO_2 included the additional transformation from CO* (2021 cm^{-1}) to *CHO (1746 cm^{-1}) (Fig. 5d) compared to Ru_1/CeO_2. After the gas flow was switched to H_2, CO* , bicarbonate, carboxylate, and *CHO quickly disappeared within 5 min (Fig. 5e). After 10 min, the band of bidentate carbonate appeared, reached its maximum strength at 15 min, and then decreased. According to the above results, adding Ni nanoparticles did not change the CO* reaction pathway of CO_2 methanation compared to Ru_1/CeO_2.

The in situ FTIR spectra for CO_2 adsorption measured at different temperatures are shown in Fig. 5f-h. For Ni/CeO_2 (Fig. 5f), the bands of the adsorbed *CHO (1740 cm^{-1}) and HCOO* (1344 cm^{-1}) species can be found in spectra [76]. In addition, the transient in situ FTIR spectra of CO_2 adsorption was recorded at 250 °C on Ni/CeO_2 (Fig. S8a). The band intensities of *CHO and HCOO* increase with time, but that of HCOO* increases more rapidly because the conversion of HCOO* to *CHO is the rate-determining step of the reaction. For Ru_1/CeO_2 (Fig. 5g), the active intermediate is only CO* , and no bands of *CHO are found with increasing temperature. After switching the gas to 10% H_2/Ar, the linear-CO* is disappeared, and the bridge-CO* is still observed (Fig. S8b). This result indicates that the linear-CO* adsorbed on the Ru single atoms is the active species, while the bridge-CO* adsorbed on CeO_2 is not, consistent with previously published literature [11]. For Ru_1Ni/CeO_2, the linear-CO* is observed in the inlet gas of CO_2, accompanied by the appearing band assigned to *CHO (Fig. 5h). Furthermore, the in situ FTIR spectra of CO* and *CHO on Ru_1Ni/CeO_2 were recorded at 200 °C with increasing time (Fig. S8c). Interestingly, the intensity of *CHO over Ru_1Ni/CeO_2 is markedly higher than that of Ni/CeO_2, which further proves the superior CO_2 activation properties of Ru_1Ni/CeO_2.

3.3.2. DFT results

To investigate and compare the roles of the Ru single atom and Ni cluster, we first calculated the adsorptions of CO and CO_2 at the surface oxygen vacancy sites near the Ru single atom or Ni cluster by the density functional theory (DFT) method (Fig. 6). As shown in Figs. 6a and 6b, the adsorption energy of CO_2 is −1.93 on Ru_1/CeO_2 and −1.22−1.22 eV on Ni/CeO_2, respectively, indicating that the CO_2 molecules are more inclined to adsorb on the oxygen vacancies that are formed near the Ru single atom compared to the Ni cluster. Furthermore, the adsorption energy of CO on the Ru single atom (Fig. 6c) is −0.78 eV, lower than that on the Ni cluster (Fig. 6d, −2.11 eV), meaning that the formed CO molecules on the Ru single atom are prone to desorb and re-adsorb on the Ni cluster.

Based on the above adsorption calculation results, the possible elementary reactions of CO and CO_2 were calculated (Fig. 7). Figs. 7a and 7b show that CO formation on the oxygen vacancy near the Ru single atom and Ni cluster needs to overcome the energy barrier of 0.78 eV and 0.94 eV, respectively. And the lower value indicates that this elementary reaction can occur more easily. After that, the possible reaction paths (CO* → C* + O*, CO* + H*→*CHO, CO* + H*→ COH*) on Ni were explored. Forming the C* and *CHO intermediates is more favorable than the COH* intermediate (Figs. 7c-7e), and its energy input is much lower than the energy needed to form *CHO on Ru single atom (Fig. S9), in agreement with the in situ FTIR results. Therefore, we believe that the Ru single atom and Ni cluster play an important role in the CO* → C* + O* and CO* + H* → *CHO routes. For Ni/CeO_2 (Fig. 7f), CO_2 molecules are hydrogenated to HCOO* by overcoming an energy barrier of 1.74 eV, much higher than that of the CO* + H* → *CHO route (1.58 eV). This result reveals that Ru_1Ni/CeO_2 with Ru

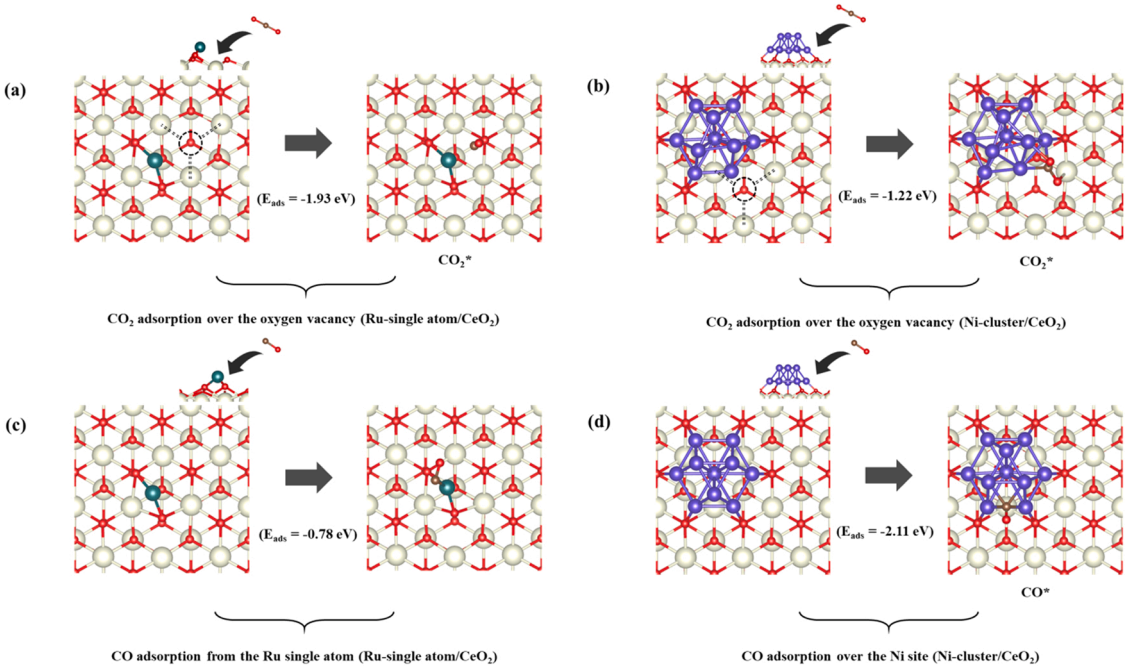

Fig. 6. The adsorption of CO_2 and CO on the different active sites: CO_2 adsorb on the oxygen vacancy near Ru single atom (a) and Ni cluster (b); CO adsorb on the Ru single atom (c) and Ni cluster (d).

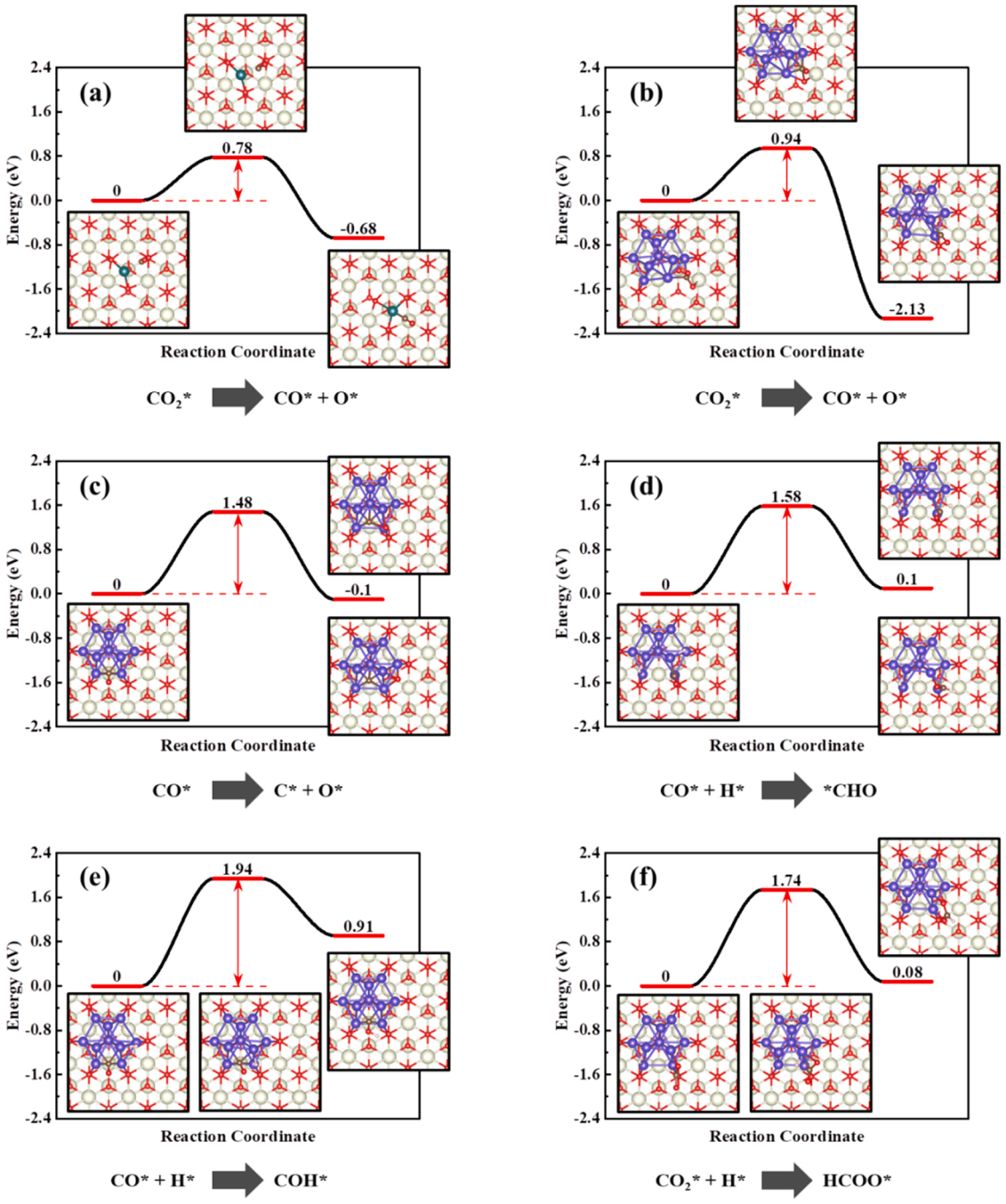

Fig. 7. The calculated energy profiles of different reaction routes. CO_2 * → CO* + O* on the oxygen vacancy near the Ru single atom (a) and Ni cluster (b); CO* → C* + O* (c), CO* + H* → CHO* (d), CO* + H* → COH* (e), and CO_2 * + H* → HCOO* (f) on the Ni cluster.

single atom and Ni cluster significantly promotes the formation of *CHO, resulting in a much-increased CO_2 methanation reaction rate.

3.3.3. *Proposed catalytic mechanism on Ru_1Ni/CeO_2*

In contrast to the Ru_1/CeO_2 +Ni/CeO_2 mixed catalyst, we demonstrated that the Ru_1Ni/CeO_2 catalyst containing two active sites (Ru_1 and Ni) is the best tandem catalyst for the CO_2 methanation reaction. This is due to the short distance between Ru_1 and Ni with competitive adsorption leading to the preferential dissociation of CO_2 to CO on the Ru_1 site. The mechanism of CO_2 methanation on Ru_1Ni/CeO_2 is proposed based on our experimental and DFT calculation results (Scheme 1): first, CO_2 is dissociated to CO on Ru single atom, after which CO hydrogenation to *CHO is accelerated on Ni, and finally, *CHO is transformed to CH_4 at the Ni site. In summary, this cascade reaction mode catalyzed by the dual active sites in Ru_1Ni/CeO_2 catalyst ensures high catalytic performance in the CO_2 methanation reaction.

4. Conclusions

The Ru_1Ni/CeO_2 catalyst with isolated Ru_1 sites and Ni nanoparticles shows much better catalytic performance in CO_2 methanation than Ru_1/CeO_2 (Ru single atom catalyst) and Ni/CeO_2 (Ni nanoparticle catalyst). Experimental and theoretical calculation results confirm that the two types of active sites (Ru_1 and Ni) in the Ru_1Ni/CeO_2 catalyst synergistically catalyze the reaction, in which the Ru_1 sites convert CO_2 into CO more effectively, whereas the Ni sites are mainly responsible for the

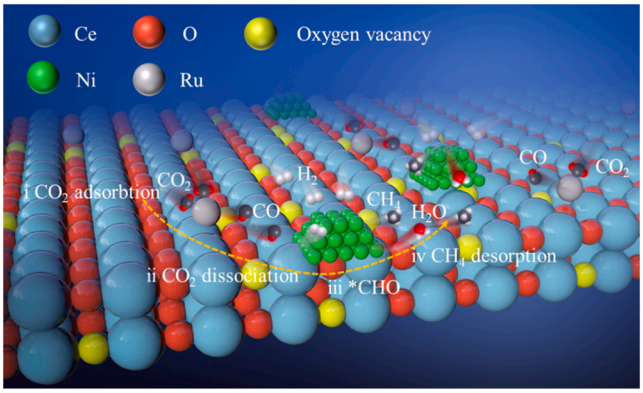

Scheme 1. Schematic illustration of CO_2 conversion to CH_4 accelerated by different reactive sites (Ru_1 and Ni).

hydrogenation of CO to CH_4. Therefore, the coexistence of the Ru and Ni sites significantly boosts the reaction as compared with their single active component catalysts. Also, the stepwise hydrogenation of CO_2 to CH_4 at different active sites is clarified experimentally and theoretically well. The reported tandem catalysts demonstrate the high possibility of boosting both the CO_2 activation and product selectivity by one catalyst.

CRediT authorship contribution statement

Tengfei Zhang: Methodology, Validation, Formal analysis, Investigation, Data curation, Writing – original draft, Visualization. **Peng Zheng:** Methodology, Software, Data curation. **Fangna Gu:** Conceptualization, Methodology, Writing – review & editing, Visualization, Supervision, Project administration. **Wenqing Xu:** Methodology, Writing – review & editing, Visualization. **Wenxing Chen:** Writing – review & editing. **Tingyu Zhu:** Writing – review & editing. **Yi-Fan Han:** Writing – review & editing. **Guangwen Xu:** Writing – review & editing. **Ziyi Zhong:** Writing – review & editing, Funding acquisition. **Fabing Su:** Writing – review & editing, Visualization, Supervision, Project administration, Funding acquisition.

Declaration of Competing Interest

The authors declare that they have no known competing financial interests or personal relationships that could have appeared to influence the work reported in this paper.

Data Availability

Data will be made available on request.

Acknowledgments

This research was funded by the National Natural Science Foundation of China (22278405 and 52222005) and the Open Project Fund from Guangdong Provincial Key Laboratory of Materials and Technology for Energy Conversion, Guangdong Technion-Israel Institute of Technology (No. MATEC2022KF0XX). Z.Z also thanks the financial support of the 2020 Li Ka Shing Foundation Cross-Disciplinary Research Grant (2020LKSFG09A).

Appendix A. Supporting information

Supplementary data associated with this article can be found in the online version at doi:10.1016/j.apcatb.2022.122190.

References

[1] F.R. Fan, R. Wang, H. Zhang, W. Wu, Emerging beyond-graphene elemental 2D materials for energy and catalysis applications, Chem. Soc. Rev. 50 (2021) 10983–11031.
[2] L. Shen, J. Xu, M. Zhu, Y.-F. Han, Essential role of the support for nickel-based CO_2 methanation catalysts, ACS Catal. 10 (2020) 14581–14591.
[3] M.C. Bacariza, D. Spataru, L. Karam, J.M. Lopes, C. Henriques, Promising catalytic systems for CO_2 hydrogenation into CH_4: a review of recent studies, Processes 8 (2020) 646.
[4] W. Li, H. Wang, X. Jiang, J. Zhu, Z. Liu, X. Guo, C. Song, A short review of recent advances in CO_2 hydrogenation to hydrocarbons over heterogeneous catalysts, RSC Adv. 8 (2018) 7651–7669.
[5] I. Sreedhar, Y. Varun, S.A. Singh, A. Venugopal, B.M. Reddy, Developmental trends in CO_2 methanation using various catalysts, Catal. Sci. Technol. 9 (2019) 4478–4504.
[6] C. Vogt, M. Monai, G.J. Kramer, B.M. Weckhuysen, The renaissance of the Sabatier reaction and its applications on Earth and in space, Nat. Catal. 2 (2019) 188–197.
[7] J. Wang, E. Kim, D.P. Kumar, A.P. Rangappa, Y. Kim, Y. Zhang, T.K. Kim, Highly durable and fully dispersed cobalt diatomic site catalysts for CO_2 photoreduction to CH_4, Angew. Chem. Int. Ed. 61 (2022), 202113044.
[8] S. Chen, Z. Zhang, W. Jiang, S. Zhang, J. Zhu, L. Wang, H. Ou, S. Zaman, L. Tan, P. Zhu, E. Zhang, P. Jiang, Y. Su, D. Wang, Y. Li, Engineering water molecules activation center on multisite electrocatalysts for enhanced CO_2 methanation, J. Am. Chem. Soc. 144 (2022) 12807–12815.
[9] D. Mateo, J. Albero, H. García, Photoassisted methanation using Cu_2O nanoparticles supported on graphene as a photocatalyst, Energy Environ. Sci. 10 (2017) 2392–2400.
[10] F. He, J. Zhuang, B. Lu, X. Liu, J. Zhang, F. Gu, M. Zhu, J. Xu, Z. Zhong, G. Xu, F. Su, Ni-based catalysts derived from Ni-Zr-Al ternary hydrotalcites show outstanding catalytic properties for low-temperature CO_2 methanation, Appl. Catal., B 293 (2021), 120218.
[11] X. Xu, L. Liu, Y. Tong, X. Fang, J. Xu, D. Jiang, X. Wang, Facile Cr^{3+}-doping strategy dramatically promoting Ru/CeO_2 for low-temperature CO_2 methanation: Unraveling the roles of surface oxygen vacancies and hydroxyl groups, ACS Catal. 11 (2021) 5762–5775.
[12] M. Zhu, P. Tian, X. Cao, J. Chen, T. Pu, B. Shi, J. Xu, J. Moon, Z. Wu, Y.-F. Han, Vacancy engineering of the nickel-based catalysts for enhanced CO_2 methanation, Appl. Catal., B 282 (2021), 119561.
[13] L. Xu, F. Wang, M. Chen, H. Yang, D. Nie, L. Qi, X. Lian, Alkaline-promoted Ni based ordered mesoporous catalysts with enhanced low-temperature catalytic activity toward CO_2 methanation, RSC Adv. 7 (2017) 18199–18210.
[14] S. Tada, O.J. Ochieng, R. Kikuchi, T. Haneda, H. Kameyama, Promotion of CO_2 methanation activity and CH_4 selectivity at low temperatures over $Ru/CeO_2/Al_2O_3$ catalysts, Int. J. Hydrog. Energy 39 (2014) 10090–10100.
[15] X. Xu, Y. Tong, J. Huang, J. Zhu, X. Fang, J. Xu, X. Wang, Insights into CO_2 methanation mechanism on cubic ZrO_2 supported Ni catalyst via a combination of experiments and DFT calculations, Fuel 283 (2021), 118867.
[16] Y. Tang, Y. Wei, Z. Wang, S. Zhang, Y. Li, L. Nguyen, Y. Li, Y. Zhou, W. Shen, F. F. Tao, P. Hu, Synergy of single-atom Ni_1 and Ru_1 sites on CeO_2 for dry reforming of CH_4, J. Am. Chem. Soc. 141 (2019) 7283–7293.
[17] W. Xing, Y. Liu, W. Zhang, Y. Sun, X. Kai, T. Yang, Study on methanation performance of biomass gasification syngas based on a Ni/Al_2O_3 monolithic catalyst, ACS Omega 5 (2020) 28597–28605.
[18] S.-I. Fujita, N. Takezawa, Difference in the selectivity of CO and CO_2 methanation reactions, Chem. Eng. J. 68 (1997) 63–68.
[19] K. Wang, Y. Men, S. Liu, J. Wang, Y. Li, Y. Tang, Z. Li, W. An, X. Pan, L. Li, Decoupling the size and support/metal loadings effect of Ni/SiO_2 catalysts for CO_2 methanation, Fuel 304 (2021), 121388.
[20] R. Zhou, N. Rui, Z. Fan, C. Liu, Effect of the structure of Ni/TiO_2 catalyst on CO_2 methanation, Int. J. Hydrog. Energy 41 (2016) 22017–22025.
[21] L. Wang, J. Hu, H. Liu, Q. Wei, D. Gong, L. Mo, H. Tao, C. Zhang, Three-dimensional mesoporous $Ni-CeO_2$ catalysts with Ni embedded in the pore walls for CO_2 methanation, Catalysts 10 (2020) 523.
[22] Y. Yan, Y. Dai, H. He, Y. Yu, Y. Yang, A novel W-doped Ni-Mg mixed oxide catalyst for CO_2 methanation, Appl. Catal. B 196 (2016) 108–116.
[23] J. Gödde, M. Merko, W. Xia, M. Muhler, Nickel nanoparticles supported on nitrogen–doped carbon nanotubes are a highly active, selective and stable CO_2 methanation catalyst, J. Energy Chem. 54 (2021) 323–331.
[24] D.C.D. da Silva, S. Letichevsky, L.E.P. Borges, L.G. Appel, The Ni/ZrO_2 catalyst and the methanation of CO and CO_2, Int. J. Hydrog. Energy 37 (2012) 8923–8928.
[25] T.A. Le, T.W. Kim, S.H. Lee, E.D. Park, CO and CO_2 methanation over Ni catalysts supported on alumina with different crystalline phases, Korean J. Chem. Eng. 34 (2017) 3085–3091.
[26] J. Ilsemann, A. Straß-Eifert, J. Friedland, L. Kiewidt, J. Thöming, M. Bäumer, R. Güttel, Cobalt@Silica core-shell catalysts for hydrogenation of CO/CO_2 mixtures to methane, ChemCatChem 11 (2019) 4884–4893.
[27] B. Miao, S.S.K. Ma, X. Wang, H. Su, S.H. Chan, Catalysis mechanisms of CO_2 and CO methanation, Catal. Sci. Technol. 6 (2016) 4048–4058.
[28] T. Abe, M. Tanizawa, K. Watanabe, A. Taguchi, CO_2 methanation property of Ru nanoparticle-loaded TiO_2 prepared by a polygonal barrel-sputtering method, Energy Environ. Sci. 2 (2009) 315–321.
[29] P.G. O'Brien, K.K. Ghuman, A.A. Jelle, A. Sandhel, T.E. Wood, J.Y.Y. Loh, J. Jia, D. Perovic, C.V. Singh, N.P. Kherani, C.A. Mims, G.A. Ozin, Enhanced photothermal reduction of gaseous CO_2 over silicon photonic crystal supported ruthenium at ambient temperature, Energy Environ. Sci. 11 (2018) 3443–3451.

[30] H. Sun, Y. Zhang, S. Guan, J. Huang, C. Wu, Direct and highly selective conversion of captured CO_2 into methane through integrated carbon capture and utilization over dual functional materials, J. CO_2 Util. 38 (2020) 262–272.
[31] R. Chein, C. Wang, Experimental study on CO_2 methanation over Ni/Al_2O_3, Ru/Al_2O_3, and Ru-Ni/Al_2O_3 catalysts, Catalysts 10 (2020) 1112.
[32] L. Merkouri, E. le Saché, L. Pastor-Pérez, M.S. Duyar, T. Ramirez Reina, Versatile Ni-Ru catalysts for gas phase CO_2 conversion: Bringing closer dry reforming, reverse water gas shift and methanation to enable end-products flexibility, Fuel 315 (2022), 123097.
[33] M.A. Paviotti, B.M. Faroldi, L.M. Cornaglia, Ni-based catalyst over rice husk-derived silica for the CO_2 methanation reaction: Effect of Ru addition, J. Environ. Chem. Eng. 9 (2021), 105173.
[34] X. Zou, Z. Shen, X. Li, Y. Cao, Q. Xia, S. Zhang, Y. Liu, L. Jiang, L. Li, L. Cui, Y. Wang, Boosting CO_2 methanation on ceria supported transition metal catalysts via chelation coupled wetness impregnation, J. Colloid Interface Sci. 620 (2022) 77–85.
[35] R. Lang, X. Du, Y. Huang, X. Jiang, Q. Zhang, Y. Guo, K. Liu, B. Qiao, A. Wang, T. Zhang, Single-atom catalysts based on the metal–oxide interaction, Chem. Rev. 120 (2020) 11986–12043.
[36] Y. Guo, S. Mei, K. Yuan, D.-J. Wang, H.-C. Liu, C.-H. Yan, Y.-W. Zhang, Low-temperature CO_2 methanation over CeO_2-supported Ru single atoms, nanoclusters, and nanoparticles competitively tuned by strong metal–support interactions and H-spillover effect, ACS Catal. 8 (2018) 6203–6215.
[37] J.H. Kwak, L. Kovarik, J. Szanyi, CO_2 reduction on supported Ru/Al_2O_3 catalysts: cluster size dependence of product selectivity, ACS Catal. 3 (2013) 2449–2455.
[38] D.-L. Meng, M.-D. Zhang, D.-H. Si, M.-J. Mao, Y. Hou, Y.-B. Huang, R. Cao, Highly selective tandem electroreduction of CO_2 to ethylene over atomically isolated nickel–nitrogen site/copper nanoparticle catalysts, Angew. Chem. Int. Ed. 60 (2021) 25485–25492.
[39] H. Zhang, X. Chang, J.G. Chen, W.A. Goddard, B. Xu, M.-J. Cheng, Q. Lu, Computational and experimental demonstrations of one-pot tandem catalysis for electrochemical carbon dioxide reduction to methane, Nat. Commun. 10 (2019) 3340.
[40] X. She, T. Zhang, Z. Li, H. Li, H. Xu, J. Wu, Tandem electrodes for carbon dioxide reduction into C2+ products at simultaneously high production efficiency and rate, Cell Rep. Phys. Sci. 1 (2020), 100051.
[41] C. Chen, Y. Li, S. Yu, S. Louisia, J. Jin, M. Li, M.B. Ross, P. Yang, Tandem catalysts for high-Rate CO_2 electrolysis toward multicarbons, Joule 4 (2020) 1688–1699.
[42] P. Liu, Z. Huang, X. Gao, X. Hong, J. Zhu, G. Wang, Y. Wu, J. Zeng, X. Zheng, Synergy between palladium single atoms and nanoparticles via hydrogen spillover for enhancing CO_2 photoreduction to CH_4, Adv. Mater. 34 (2022), 2200057.
[43] N. Hashimoto, K. Mori, K. Asahara, S. Shibata, H. Jida, Y. Kuwahara, H. Yamashita, How the morphology of NiO_x-decorated CeO_2 nanostructures affects catalytic properties in CO_2 methanation, Langmuir 37 (2021) 5376–5384.
[44] B. Ravel, M. Newville, ATHENA, ARTEMIS, HEPHAESTUS: data analysis for X-ray absorption spectroscopy using IFEFFIT, J. Synchrotron Radiat. 12 (2005) 537–541.
[45] T. Zhang, Q. Liu, Lanthanum-modified MCF-derived nickel phyllosilicate catalyst for enhanced CO_2 methanation: a comprehensive study, ACS Appl. Mater. Interfaces 12 (2020) 19587–19600.
[46] G. Kresse, J. Furthmüller, Efficient iterative schemes for ab initio total-energy calculations using a plane-wave basis set, Phys. Rev. B Condens Matter 54 (1996) 11169–11186.
[47] G. Kresse, J. Furthmüller, Efficiency of ab-initio total energy calculations for metals and semiconductors using a plane-wave basis set, Comput. Mater. Sci. 6 (1996) 15–50.
[48] J.P. Perdew, K. Burke, M. Ernzerhof, Generalized gradient approximation made simple, Phys. Rev. Lett. 77 (1996) 3865–3868.
[49] S. Grimme, J. Antony, S. Ehrlich, H. Krieg, A consistent and accurate ab initio parametrization of density functional dispersion correction (DFT-D) for the 94 elements H-Pu, J. Chem. Phys. 132 (2010), 154104.
[50] S.L. Dudarev, G.A. Botton, S.Y. Savrasov, C.J. Humphreys, A.P. Sutton, Electron-energy-loss spectra and the structural stability of nickel oxide: an LSDA+U study, Phys. Rev. B 57 (1998) 1505–1509.
[51] G. Henkelman, H. Jónsson, Improved tangent estimate in the nudged elastic band method for finding minimum energy paths and saddle points, J. Chem. Phys. 113 (2000) 9978–9985.
[52] T. Zhang, W. Wang, F. Gu, W. Xu, J. Zhang, Z. Li, T. Zhu, G. Xu, Z. Zhong, F. Su, Enhancing the low-temperature CO_2 methanation over Ni/La-CeO_2 catalyst: The effects of surface oxygen vacancy and basic site on the catalytic performance, Appl. Catal. B 312 (2022), 121385.
[53] B. Hu, K. Sun, Z. Zhuang, Z. Chen, S. Liu, W.-C. Cheong, C. Chen, M. Hu, X. Cao, J. Ma, R. Tu, X. Zheng, H. Xiao, X. Chen, Y. Cui, Q. Peng, C. Chen, Y. Li, Distinct crystal-facet-dependent behaviors for single-atom palladium-on-ceria catalysts: enhanced stabilization and catalytic properties, Adv. Mater. 34 (2022), 2107721.
[54] P. Ji, J. Zhang, F. Chen, M. Anpo, Ordered mesoporous CeO_2 synthesized by nanocasting from cubic Ia3d mesoporous MCM-48 silica: Formation, characterization and photocatalytic activity, J. Phys. Chem. C 112 (2008) 17809–17813.
[55] W. Shan, M. Luo, P. Ying, W. Shen, C. Li, Reduction property and catalytic activity of $Ce_{1-x}Ni_xO_2$ mixed oxide catalysts for CH_4 oxidation, Appl. Catal. A 246 (2003) 1–9.
[56] L.M.N.C. Alves, M.P. Almeida, M. Ayala, C.D. Watson, G. Jacobs, R.C. Rabelo-Neto, F.B. Noronha, L.V. Mattos, CO_2 methanation over metal catalysts supported on ZrO_2: Effect of the nature of the metallic phase on catalytic performance, Chem. Eng. Sci. 239 (2021), 116604.
[57] G. Zhou, H. Liu, K. Cui, A. Jia, G. Hu, Z. Jiao, Y. Liu, X. Zhang, Role of surface Ni and Ce species of Ni/CeO_2 catalyst in CO_2 methanation, Appl. Surf. Sci. 383 (2016) 248–252.
[58] M.L. Ang, U. Oemar, Y. Kathiraser, E.T. Saw, C.H.K. Lew, Y. Du, A. Borgna, S. Kawi, High-temperature water–gas shift reaction over Ni/xK/CeO_2 catalysts: Suppression of methanation via formation of bridging carbonyls, J. Catal. 329 (2015) 130–143.
[59] P. Hongmanorom, J. Ashok, P. Chirawatkul, S. Kawi, Interfacial synergistic catalysis over Ni nanoparticles encapsulated in mesoporous ceria for CO_2 methanation, Appl. Catal. B 297 (2021), 120454.
[60] N. Wang, W. Qian, W. Chu, F. Wei, Crystal-plane effect of nanoscale CeO_2 on the catalytic performance of Ni/CeO_2 catalysts for methane dry reforming, Catal. Sci. Technol. 6 (2016) 3594–3605.
[61] R. Murugan, G. Ravi, G. Vijayaprasath, S. Rajendran, M. Thaiyan, M. Nallappan, M. Gopalan, Y. Hayakawa, Ni–CeO_2 spherical nanostructures for magnetic and electrochemical supercapacitor applications, Phys. Chem. Chem. Phys. 19 (2017) 4396–4404.
[62] T. Wang, X. Tao, X. Li, K. Zhang, S. Liu, B. Li, Synergistic Pd single atoms, clusters, and oxygen vacancies on TiO_2 for photocatalytic hydrogen evolution coupled with selective organic oxidation, Small 17 (2021), 2006255.
[63] A. Cárdenas-Arenas, A. Quindimil, A. Davó-Quiñonero, E. Bailón-García, D. Lozano-Castelló, U. De-La-Torre, B. Pereda-Ayo, J.A. González-Marcos, J. R. González-Velasco, A. Bueno-López, Design of active sites in Ni/CeO_2 catalysts for the methanation of CO_2: tailoring the Ni-CeO_2 contact, Appl. Mater. Today 19 (2020), 100591.
[64] L. Xu, F. Wang, M. Chen, D. Nie, X. Lian, Z. Lu, H. Chen, K. Zhang, P. Ge, CO_2 methanation over rare earth doped Ni based mesoporous catalysts with intensified low-temperature activity, Int. J. Hydrog. Energy 42 (2017) 15523–15539.
[65] H. Nagase, R. Naito, S. Tada, R. Kikuchi, K. Fujiwara, M. Nishijima, T. Honma, Ru nanoparticles supported on amorphous ZrO_2 for CO_2 methanation, Catal. Sci. Technol. 10 (2020) 4522–4531.
[66] C. Fukuhara, K. Hayakawa, Y. Suzuki, W. Kawasaki, R. Watanabe, A novel nickel-based structured catalyst for CO_2 methanation: a honeycomb-type Ni/CeO_2 catalyst to transform greenhouse gas into useful resources, Appl. Catal. A 532 (2017) 12–18.
[67] Q. Liu, S. Wang, G. Zhao, H. Yang, M. Yuan, X. An, H. Zhou, Y. Qiao, Y. Tian, CO_2 methanation over ordered mesoporous NiRu-doped CaO-Al_2O_3 nanocomposites with enhanced catalytic performance, Int. J. Hydrog. Energy 43 (2018) 239–250.
[68] Q. Liu, F. Gu, X. Lu, Y. Liu, H. Li, Z. Zhong, G. Xu, F. Su, Enhanced catalytic performances of Ni/Al_2O_3 catalyst via addition of V_2O_3 for CO methanation, Appl. Catal., A 488 (2014) 37–47.
[69] C. Binet, M. Daturi, J.-C. Lavalley, IR study of polycrystalline ceria properties in oxidised and reduced states, Catal. Today 50 (1999) 207–225.
[70] S.Y. Chin, C.T. Williams, M.D. Amiridis, FTIR studies of CO adsorption on Al_2O_3- and SiO_2-supported Ru catalysts, J. Phys. Chem. B 110 (2006) 871–882.
[71] A. Comas-Vives, K. Furman, D. Gajan, M.C. Akatay, A. Lesage, F.H. Ribeiro, C. Copéret, Predictive morphology, stoichiometry and structure of surface species in supported Ru nanoparticles under H_2 and CO atmospheres from combined experimental and DFT studies, Phys. Chem. Chem. Phys.. 18 (2016) 1969–1979.
[72] M.G. Musolino, C.V. Caia, C. Busacca, F. Mauriello, R. Pietropaolo, Selective conversion of cis-2-butene-1,4-diol to 2-hydroxytetrahydrofuran over K, Ca and Ba metals-promoted Ru/SiO_2 catalysts: Role of the promoter, Appl. Catal. A 357 (2009) 106–113.
[73] C. Li, Y. Sakata, T. Arai, K. Domen, K.I. Maruya, T. Onishi, Adsorption of carbon monoxide and carbon dioxide on cerium oxide studied by Fourier-transform infrared spectroscopy. Part 2.—Formation of formate species on partially reduced CeO_2 at room temperature, J. Chem. Soc., Faraday Trans. 85 (1989) 1451–1461.
[74] O. Pozdnyakova, D. Teschner, A. Wootsch, J. Kröhnert, B. Steinhauer, H. Sauer, L. Toth, F.C. Jentoft, A. Knop-Gericke, Z. Paál, R. Schlögl, Preferential CO oxidation in hydrogen (PROX) on ceria-supported catalysts, part I: Oxidation state and surface species on Pt/CeO_2 under reaction conditions, J. Catal. 237 (2006) 1–16.
[75] X. Zhou, J. Shan, L. Chen, B.Y. Xia, T. Ling, J. Duan, Y. Jiao, Y. Zheng, S.-Z. Qiao, Stabilizing Cu^{2+} ions by solid solutions to promote CO_2 electroreduction to methane, J. Am. Chem. Soc. 144 (2022) 2079–2084.
[76] T. Jin, Y. Zhou, G.J. Mains, J.M. White, Infrared and x-ray photoelectron spectroscopy study of carbon monoxide and carbon dioxide on platinum/ceria, J. Phys. Chem. 91 (1987) 5931–5937.